



Monitoring Urban Heat Island Intensity with Ground-based GNSS Observations and  
Space-based Radio Occultation and Radiosonde Historical Data

Pengfei Xia<sup>1</sup>, Wei Peng<sup>2</sup>, Shirong Ye<sup>1</sup>, Min Guo<sup>3</sup>, Fangxin Hu<sup>1</sup>

<sup>1</sup>GNSS Research Center, Wuhan University, Wuhan 430079, China

<sup>2</sup>Faculty of Engineering and applied science, University of Regina, Regina, Saskatchewan,  
Canada

<sup>3</sup> School of Surveying and Land Information Engineering, Henan Polytechnic University, Jiaozuo  
454000, China

Correspondence to: Pengfei Xia( [xpf130@163.com](mailto:xpf130@163.com) )

**Abstract.** Since Urban Heat Islands (UHI) not only negatively impact human health but consume more energy when cooling buildings, accurate monitoring of its impact is critical. In this study, we propose a ground based GNSS technique to fuse GNSS Radio Occultation (RO) and radiosonde products to monitor the UHI intensity, which described as follows: First, the first and second grid tops are defined using the historical RO and radiosonde products. Then, the wet refractivity between the first and second grid tops is fitted to the higher-order spherical harmonic function based on the RO and radiosonde products, and they are used as the inputs of GNSS tomography, which can reduce the number of unknowns voxels of tomography while increasing the effective number of satellite rays, and improving the accuracy of tomography results. Next, according to the relationships among wet refractivity, temperature, and water vapor partial, as well as the function relationships among temperature, wet pressure, and height in adjacent vertical layers, the temperature and water vapor partial pressure can be obtained using the best search method according to the tomography-derived wet refractivity. Finally, the UHI intensity is monitored by the temperature difference between the urban regions and the surrounding rural regions. The radio occultation and radiosonde products of the Hong Kong region from 2010 to 2019, and the observed GNSS network data of the Hong Kong region for the year of 2020 are employed to evaluate the UHI intensity algorithm. The validation of the algorithm is done by comparing the UHI intensity estimated from the algorithm with the temperature data obtained from weather stations. The result shows that the proposed algorithm can achieve an accuracy of 1.2 K at a 95% confidence level.

**Keywords:** Urban heat island (UHI), GNSS, Tomography, Temperature

## 1. Introduction

The urban heat island (UHI) effect arises as urban regions become warmer than their rural environments (Roth, 2013). The UHI is mainly caused by heat absorbed by built structures and anthropogenic heat sources in cities (Roth, 2013). The UHI intensity is related to many factors such as regional climate, urbanization, and topography, etc. Since the 21st century, with the rapid development of urbanization, densified urban building clusters, and a large number of people gathering in cities, the increases in industrial production and domestic energy use have intensified the UHI effect, leading to a continuous expansion of its scope and intensity (Zhai et al., 2018; Xu et al., 2018; Zou et al., 2019; Jiang et al., 2019). The heat island effect severely affects the life of citizens and even the overall ecological quality of cities, because it increases the heat stress of citizens, which further triggers cardiovascular, respiratory and mental diseases, resulting in increased morbidity and mortality worldwide. The study of the urban heat island formation and evolution, spatial and temporal distribution, causal mechanisms and the search for effective mitigation measures have become the focus of attention of many scholars in recent years (Rizwan



et al., 2008; Memon et al., 2009; Azevedo and Leal, 2017; Lamarca et al., 2018).

Traditionally, three techniques are used to monitor the UHI intensity: a network of ground-based temperature sensors (Ramamurthy and Sangobanwo, 2016); remote Sensing Satellite data (Schwarz et al., 2011; Wu et al., 2014; Fang et al., 2016; Kayet et al., 2016) and airborne instruments (Peng et al., 2017). The above observation methods have some drawbacks such as low spatial resolutions, high cost and weather dependence (Jorge et al., 2021). For example, when temperature sensors are used to obtain the relevant patterns, it is mainly to compare the temperatures of urban and suburban areas during the same period, but due to the limited monitoring points, it is difficult to reflect the UHI effect of the study area comprehensively. To address this issue, a wide metropolitan area has been covered by a dense sensor network, which no doubt leads to increased monitoring costs (Jauregui, 1997; Jin, 2012). Satellite imaging and airborne instruments require clear-sky conditions to obtain accurate data (Grimmond et al., 2010; Vahmani and Ban-Weiss, 2016). GNSS (Global Navigation Satellite Systems) technology, a new means of atmospheric sounding, can not only effectively overcome the shortcomings of traditional means (i.e., can compensate for these disadvantages), but also has the advantages of high observation accuracy, quasi-real-time, all-weather, no need for human interference, no need for instrument calibration, etc (Kouba and Héroux, 2001; Cai et al., 2013 and 2015).

A novel method of monitoring the UHI intensity using GNSS data was first presented by Jorge et al (2021). This algorithm is based on the relationship between the single GNSS-derived Zenith Tropospheric Delay (ZTD) and the environmental variables (pressure, water vapor partial pressure, and temperature) at the measurement site. The UHI intensity is calculated by subtracting the temperature at an urban GNSS station from the temperature at a rural GNSS station. However, due to the limited number of GNSS stations in each city, the single-station GNSS inversion of atmospheric temperature cannot be used for the heat island effect in urban areas. In recent years, the GNSS tomography technique has been applied as an effective means to acquire the three-dimensional (3-D) distribution of wet refractivity and can compensate for single GNSS algorithm's disadvantages. In order to monitor the UHI intensity, it is necessary to estimate the temperature from GNSS-derived wet refractivity (Troller et al., 2006; Bender et al., 2011; Lutz et al., 2010; Rohm, 2013; Chen et al., 2014; Xia et al., 2018). Therefore, the quality of the wet refractivity determines the accuracy of the temperature inversion.

The key advantage of the GNSS tomography technique over the single GNSS method is that it can obtain the three-dimensional distribution of the temperature in the study area, and can study the temperature changes in the horizontal direction and vertical direction. The second advantage is that it can promote the application scope of GNSS sensors. The proposed paper developed an optimized method for GNSS 3-D troposphere tomography using the external radiosonde and GNSS radio occultation (RO) historical data. Among them, the radiosonde and RO products are utilized to determine the first grid top and the second grid top for the purpose of grid division. Further, the wet refractivity is obtained between the first grid top and the second grid based on radiosonde and RO data which are used as the input value of the GNSS tomography. Next, the temperature can be obtained using the optical search method from tomography-derived wet refractivity. The ground-based GNSS observation data from the Hong Kong SatRef network in 2020 are used to verify the feasibility and superiority of the optimized tomography method. In addition, the temperature from 5 weather stations in Hong Kong is selected as a reference to validate the temperatures obtained by GNSS data.



88 The paper is organized as follows: In section 2, the method development is presented. Then,  
89 Section 3 describes the processing of the data, before the discussions in Section 4, followed by the  
90 conclusions in Section 5.

## 91 2. Methodology

92 This section introduces the basic tomography model; describes the tomography grid division and  
93 the calculation of temperature from wet refractivity; and presents the calculations of the UHI  
94 intensity from temperature.

### 95 2.1 Tomography model

96 The SWD along the ray paths traversing the imaging region should first be derived from the dual-  
97 frequency GNSS data to reconstruct the 3D images of the atmospheric wet refractivity distributions,  
98 which is defined by the line integral of  $N_w$  along the ray path from the satellite to the receiver (Flores  
99 et al., 2001) as follows:

$$100 \quad \text{SWD} = 10^{-6} \cdot \int_{h_0}^{\infty} N_w \cdot dh \quad (1)$$

$$101 \quad \text{SWD} = 10^{-6} \cdot \sum_{i=1}^m \sum_{j=0}^4 C_{i,j}^4 \cdot N_w(s_j^i) = S \cdot N_w + \Delta_{\text{SWD}} \quad (2)$$

102 where,  $C_{i,j}^4$  is the 4-order coefficients of the  $j$ -th segment point within the  $i$ -th grid;  $N_w(s_j^i)$  is the  
103 corresponding atmospheric wet refractivity;  $m$  denotes the number of the grids which the signals had  
104 passed;  $S$  represents the distance of the GNSS signals spanning the voxel, and  $\Delta_{\text{SWD}}$  is the noise.

105 Due to the near-cone geometry of GNSS observations (Bender and Raabe, 2007; Benevides et al.,  
106 2016), the GNSS signal cannot pass through all voxels, which resulted in too many zeros in the  
107 design matrix, and the tomographic system cannot be inverted. Therefore, it is necessary to apply  
108 appropriate constraints to overcome this issue. Though the Gauss weighted method (Song, 2004) can  
109 be used for the horizontal direction, the vertical distribution is still modeled by an exponential  
110 equation, taking account of the water vapor in the vertical direction ( which usually decreases with  
111 increasing height) as follows:

$$112 \quad N_w(h) = N_c \cdot e^{\left(-\frac{(h-h_0)}{H_z}\right)} \quad (3)$$

113 where,  $N_w(h)$  denotes the atmospheric wet refractivity at the height of  $h$ ;  $H_z$  represents the height  
114 index of  $N_w$ ;  $N_c$  is the constant value;  $h_0$  is a constant. Based on Eq. (3), Eq. (4) is employed as the  
115 vertical constraint to establish the relationship between atmospheric wet refractivity in adjacent  
116 vertical layers:

$$117 \quad \frac{N_w^{i,j,k+1}}{N_w^{i,j,k}} = e^{\left(\frac{h_k - h_{k+1}}{H_z}\right)} \quad (4)$$

118 where, the subscripts “ $i$ ”, “ $j$ ”, and “ $k$ ” define the indexes of the voxels in the east-west, north-south,  
119 and vertical directions, respectively;  $h_k$  is the height of the  $k^{\text{th}}$  voxel. Thus, the tomography equation  
120 can be solved by adopting Kalman filtering based on the horizontal and vertical constraints.

### 121 2.2 Tomography grid division

122 Generally, both the lower and upper limits of the tomographic grid refer to the height from the  
123 ground to the top of the tropopause. However, the wet refractivity is mostly clustered at a height that  
124 significantly below the tropopause. If the top of grid uses tropopause, the solutions of the  
125 tomography inversion may be negative since the wet refractivity is very sparse near the height of the  
126 tropopause (Flores et al., 2000). Two grid heights in this study are defined according to the ZWD  
127 variations obtained from radiosonde and Radio occultation data. The first grid top is the upper limit



of the tomography grid, but when the tomography equation cannot calculate the  $N_w$  value between the first and the second grid tops, the radiosonde-derived  $N_w$  or RO-derived  $N_w$  are used to take its place. As a result, when the height of the grid top decreases, the effective number of satellite rays increases. In the tomography, the rays penetrating the grid from the top boundary are the only rays used in the tomographic solution.

GNSS tomography aims to reconstruct the vertical distribution of  $N_w$ . The division of the vertical grid severely affects the tomography solutions. Conventionally, two approaches have been used for dividing the grid: the uniform division (Flores et al., 2000; Xia et al., 2013 and 2018) and non-uniform division (Perler et al., 2011; Rohm, 2012 and Jiang et al., 2014). Considering the practical distribution characteristics of  $N_w$  are sparse in high layers and dense in low layers, the non-uniform division is used here.

### 2.3 Calculation of temperature from $N_w$

The ZWD is related to the environmental conditions because of the wet refractivity of the troposphere. The wet refractivity  $N_w$  of the troposphere is defined as:

$$N_w = \left(k_2 - k_1 \frac{R_d}{R_w}\right) \cdot \frac{P_w}{T} + k_3 \cdot \frac{P_w}{T^2} \quad (5)$$

where, the empirically calculated constants  $k_1=77.6$ ,  $k_2=72$ , and  $k_3=3.75 \times 10^5$ ;  $R_d$  and  $R_w$  are mean specific gas constant for dry air and water vapor, respectively;  $P_w$  is the water vapor partial pressure, and  $T$  is the temperature in Kelvins.

The temperature of the grid point is calculated by putting zero to the equation of wet refractivity (Eq.5) and solving the quadratic equation:

$$T^2 \cdot N_w - T \cdot \left(k_2 - k_1 \frac{R_d}{R_w}\right) \cdot P_w - k_3 \cdot P_w = 0 \quad (6)$$

Although the  $N_w$  can be obtained from the above tomography equation, the  $P_w$  and  $T$  cannot be solved directly because the equation (6) is rank deficient. Therefore, Eq. (6) requires additional conditions to calculate  $P_w$  and  $T$ .

In the vertical direction, the temperature decreases with height at a relatively consistent rate and denoting the lapse rate  $\beta$ , we have

$$T_{i+1} = T_i - \beta \cdot (h_{i+1} - h_i) \quad (7)$$

where,  $T_i$ ,  $T_{i+1}$  represent the temperature at the  $i^{th}$  and  $(i+1)^{th}$  grids, respectively;  $h_i$ ,  $h_{i+1}$  represent the height at the  $i^{th}$  and  $(i+1)^{th}$  grids, respectively.

The water vapor partial pressure usually decreases with height, and it can be expressed as an empirical exponential function (Callahan, 1973):

$$P_w^{i+1} = P_w^i \cdot \exp(a \cdot (h_{i+1} - h_i) - b \cdot (h_{i+1} - h_i)^2) \quad (8)$$

where,  $P_w^i$ ,  $P_w^{i+1}$  represent the water vapor partial pressure at the  $i^{th}$  and  $(i+1)^{th}$  grids, respectively;  $a$  and  $b$  are constant, which can be obtained based on radiosonde and RO products.

Combining Equations (6), (7) and (8), the search ranges for water vapor partial pressure and temperature are given based on radiosonde data, and then the optimal water vapor partial pressure and temperature are searched.

### 2.4 Calculation of the UHI intensity

The UHI can be calculated by estimating the temperature difference between urban and rural grid points based on ground-based GNSS tomography technique. Eq. (9) shows the calculations:



$$UHII_{GNSS} = T_{GNSS}(urban) - T_{GNSS}(rural) \quad (9)$$

where,  $T_{GNSS}$  is the temperature in Kelvins obtained from GNSS tomography. The algorithm usually can be validated by comparing the UHII obtained using GNSS data with the UHII obtained using meteorological data.

$$UHII_{Met} = T_{Met}(urban) - T_{Met}(rural) \quad (10)$$

where,  $T_{Met}$  is the temperature obtained from meteorological data.

### 3 Processing results and analysis

#### 3.1 Data description

Since 2001, there has been a substantial supply of continuous temperature and pressure measurements provided by the satellite-based GNSS RO data with high accuracy, high vertical resolution, and global coverage as a function of altitude in the upper troposphere and lower stratosphere. In this paper, we used the most recent Wegener Center (WEGC) multi-satellite GNSS RO data, OPSv5.6, from May 2001 to December 2020. WEGC OPSv5.6 has been widely used for weather, climate, space weather, and geodetic studies as it provides global upper-air satellite data in high quality from multiple RO satellite missions, which including CHAMP, GRACE, SAC-C, Formosat-3/COSMIC, and Metop (Schreiner et al., 2007; Anthes et al. 2008). The radiosonde technique is a tool for studying meteorology from the ground to the lower stratosphere. RO and radiosonde observations are key data sources for weather studies and climate analysis (Kuo et al., 2005; Kishore et al., 2011).

The Ground-based GNSS observation data are obtained from the Hong Kong Satellite Navigation System (HKSN) network, which is composed of 12 continuously operating stations with a distance of 10-15 km between stations, as shown in Fig. 1. All 18 stations are provided by "LEICA GRX1200+GNSS" receivers with a data sampling rate of 5s. The 2020 one-year GNSS dataset is collected in Hong Kong. Additionally, the RO wet profiles with the same Hong Kong address and the radiosonde products at the "45004th" station from 2010 to 2019 are utilized as historical data for optimization of tomographic solutions.

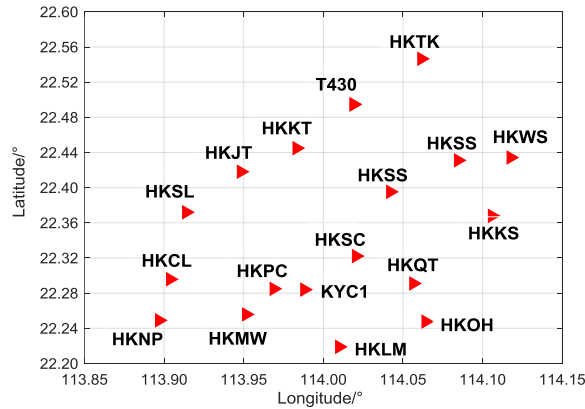


Fig.1. The GNSS station distribution and horizontal grid division in Hong Kong

A sliding time window strategy is a great approach for the simulation of near real-time GNSS tomographic experiment (Foster et al., 2005). Furthermore, providing a logical time interval is



meaningful in the framework of the rain now-casting. Moreover, a 6h time interval for the minimum broken line length is recommended empirically to allow the linear fitting algorithm can conduct a better discretization of the PWV signal features without being affected by the noisy features (Benevides et al., 2015). Therefore, a six-hour interval's time window is used, moving forward by an hour each time. The GAMIT software is used in this study to obtain ZTD (Herring et al., 2010).

### 3.2 Defining the grid top

In the zenith direction, the wet tropospheric delay can be expressed as:

$$ZWD_h = 10^{-6} \int_h^{\infty} N_w \cdot d_h \quad (11)$$

where,  $ZWD_h$  is the wet tropospheric delay (unit: m);  $h$  is the height of the observation station over mean sea level (unit: m);  $N_w$  is the atmospheric wet refractivity (unitless) that can be modeled from Eq.(5).

In this study, the ZWD is obtained from radiosonde data and RO profiles. They are used to define the grid top. The radiosonde sensors can measure several meteorological parameters such as pressure, temperature, and relative humidity. Similar to radiosonde, RO profiles also provide meteorological products such as temperature, water vapor pressure, etc. Taking the characteristic of exponential decreasing of the atmospheric refractivity into account, the formulas for wet delays from the radiosonde measurements and RO profiles can be derived:

$$ZWD_h = 10^{-6} \sum_i [(h_i - h_{i+1})(N_w^{i+1} - N_w^i) / (\ln N_w^i - \ln N_w^{i+1})] \quad (12)$$

Afterward, slant wet delay (SWD) can be obtained from ZWD based on the wet Niell mapping function (Niell, 1996).

$$SWD_h = ZWD_h \cdot M_w^{\text{Niell}}(e_{\min}) \quad (13)$$

where,  $M_w^{\text{Niell}}$  is the wet Niell mapping function;  $e_{\min}$  means the minimum satellite cut-off angle, which is  $10^\circ$  in this study. When the  $SWD_h$  is less than or equal to 1 mm, the corresponding height is defined as the first grid top (FGT). The difference between ZWD and  $N_w$  between two adjacent time periods can be calculated:

$$\Delta ZWD_h^t = |ZWD_h^t - ZWD_h^{t+1}| \quad (14)$$

$$\text{RMSN} = \sqrt{\frac{\sum_{i=1}^n (N_w^{h_{i,t}} - N_w^{h_{i,t+1}})^2}{n}} \quad (15)$$

where,  $ZWD_h^t$  and  $ZWD_h^{t+1}$  are the ZWD at height  $h$  at time  $t$  and  $t+1$ , respectively.  $N_w^{h_{i,t}}$  and  $N_w^{h_{i,t+1}}$  are the height  $h$  at time  $t$  and  $t+1$ ;  $n$  is the number of the layers of radiosonde and RO data. When the  $\Delta ZWD_h^t$  is less than or equal to 0.5 mm or RMSN is less than or equal to 0.5N, the corresponding height is defined as the second grid top (SGT).

RO wet profile and radiosonde products at the “45004th” station from 2010 to 2019 are used to determine the grid top based on Equations (13), (14) and (15). Individual radiosonde data, which have different vertical resolutions, are linearly interpolated to a 100-m vertical grid before the grid top identification. Then, we compute the daily mean for the first grid top and the second grid top as shown in Figure 2.

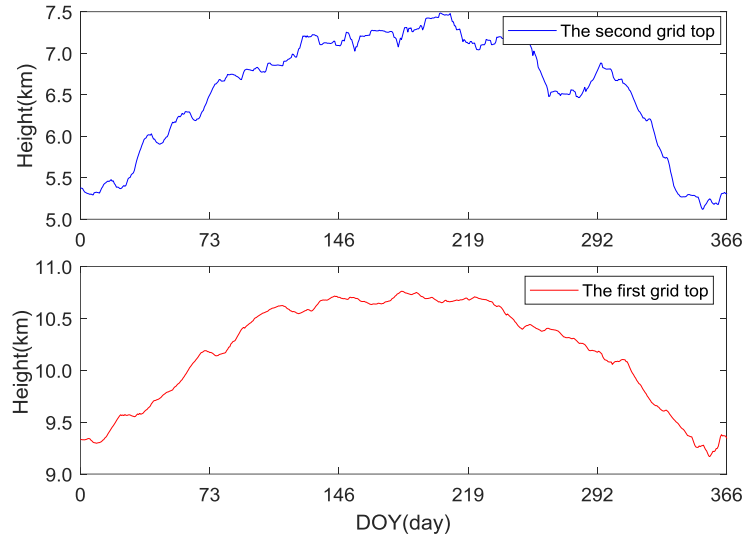


Figure 2. The first grid top and the second grid top obtained by radiosonde and RO products.

It can be seen from Figure 2 that FGT and SGT are significantly higher in summer than in spring and winter. Compared with spring and winter, the SGT is 1-2 km higher in summer than in spring and winter, while the FGT is 0.5-1.5 km higher in summer than in spring and winter. The variation of the two grid heights with time is a non-smooth curve, and the SGT is more jittered than the first grid height. Thus, we divide the vertical layers into three stages. The first stage is from the ground to 1km, which be further divided into 3 layers: the heights of the first two layers are 300m, and the height of the third layer is 400m. The second stage is from 1km to SGT. The grid in this stage is divided into an even vertical height which requires the height of a grid is no less than 400m and not more than 600m. The last stage is from the SGT to the FGT. The grid in this stage is divided into an even vertical height which requires the height of the grid is no less than 600m, and not greater than 1000m.

### 3.3 Obtaining the $N_w$ between FGT and SGT

The RO wet profile and Radiosonde product have been quality controlled, and  $N_w$  can be obtained from the water vapor pressure and temperature provided by the two meteorological data in equation (5). We add daily and semidiurnal terms to the annual and semiannual cycle variation characteristics of  $N_w$ , and the  $N_w$  time series obtained by the following equation which is layered for periodic fitting (from 5km to 11km, it is divided into 12 layers on average, that is, a layer of 500m).

$$N_w^j = \sum_{n=0}^2 a_n^j \cos\left(2n\pi \frac{\text{doy}-b_n^j}{365.25}\right) + \sum_{n=3}^4 a_n^j \cos\left(2(n-2)\pi \frac{\text{hod}-b_n^j}{24}\right) \quad (16)$$

where,  $j$  is the number of layers;  $N_w^j$  is the wet refractivity of the  $j^{\text{th}}$  layer; doy is the annual cumulative day; hod is the UTC time;  $a_n$  ( $n=0,1,2$ ) is the annual mean; annual cycle variation amplitude and semiannual cycle variation amplitude of  $N_w$ ,  $b_n$  ( $n=1,2$ ) is the annual cycle variation initial phase and semiannual cycle variation initial phase;  $a_n$  ( $n=3,4$ ) is the daily cycle variation amplitude and semiannual cycle variation amplitude;  $b_n$  ( $n=3,4$ ) is the daily cycle variation initial phase and semiannual cycle variation initial phase, respectively. The values of  $a_n$  and  $b_n$  in Eq.(16)



at different altitude levels can be fitted by selecting the RO and radiosonde products in Hong Kong from 2010 to 2019.

SWD is the input value of the GNSS tomography technique, and its accuracy directly affects the accuracy of tomography-derived  $N_w$ . To evaluate the fitting accuracy of  $N_w$  between SGT and FGT, we selected the 2020 Hong Kong area radiosonde and RO products as the benchmark values. The difference of SWD can be obtained between benchmark value and  $N_w$  for different seasons derived from Eq. (16), as shown in Eq. (17). The statistical results are displayed in Table 1.

$$\Delta\text{SWD}_{SGP}^{FGP} = (\text{ZWD}_{model} - \text{ZWD}_T) \cdot M_w^{\text{Niell}}(e) \quad (17)$$

where,  $\text{ZWD}_{model}$  denotes the ZWD obtained from Eq. (5) and Eq. (16);  $\text{ZWD}_T$  denotes the ZWD estimated from RO and radiosonde products using Eq. (5);  $e$  is the satellite cut-off angle;  $M_w^{\text{Niell}}$  is the Niell wet projection function.

**Table 1.** Results of the differences of SWD between model-derived and benchmark values at different cut-off angles (Unit mm).

Cut-off angle	Spring	Summer	Autumn	Winter
7°-15°	3.6	5.1	2.7	2.2
15°-30°	1.5	2.2	1.4	1.2
30°-45°	0.9	1.2	0.9	0.8
45°-60°	0.7	0.9	0.6	0.6
60°-75°	0.6	0.8	0.6	0.5
75°-90°	0.5	0.7	0.5	0.5

Table 1 shows that the value of  $\Delta\text{SWD}_{SGP}^{FGP}$  is significantly larger at lower satellite cut-off angles. In addition,  $\Delta\text{SWD}_{SGP}^{FGP}$  is significantly larger in summer than in other seasons, with a deviation of more than 5mm. At satellite cut-off angles above 45°, the effect of  $\Delta\text{SWD}_{SGP}^{FGP}$  is less than 1mm, while at satellite cut-off angles below 30°, the effect of  $\Delta\text{SWD}_{SGP}^{FGP}$  is greater than 1mm.

#### 4. Discussion

The 450045<sup>th</sup> radiosonde station was carried aloft once every 12h in Hong Kong, and it was equipped with a configured sensor that collects information about temperature, pressure, relative humidity and so on. Here, the 450045<sup>th</sup> radiosonde products in 2020 were used to evaluate the accuracy of the tomography results. These products were further used to validate the accuracy of the temperature obtained from  $N_w$ .

##### 4.1 GNSS tomographic results

We utilized GAMIT software to obtain the ZTD based on GNSS data from the Hong Kong SatRef network with IGS (International GNSS Service) ultra-rapid products orbit file. The Saastamoinen model and GPT3 model were used to obtain the ZHD and then the ZWD was obtained by deducting the ZHD from the ZTD. The SWD was computed from ZWD using Niell wet mapping function. Finally, we estimated the 3-D distribution of atmospheric wet refractivity using parameterized approaches, in which Eq. (16) was used for deriving the  $N_w$  between SGT and FGT. Besides, Kalman filtering algorithm was used for tomography solutions.

To evaluate our optimized method, the tomography results were compared with those derived from the traditional tomography method, in which the atmospheric wet refractivity from SGT to FGT was estimated as unknown. First, the numbers of signals passing through the voxel (NSV) were compared when the optimized method and traditional method were used to invert the  $N_w$  given in Figure 3. Then, tomography solutions were compared with external results derived from the



298 radiosonde. The results are shown in Figure 3.

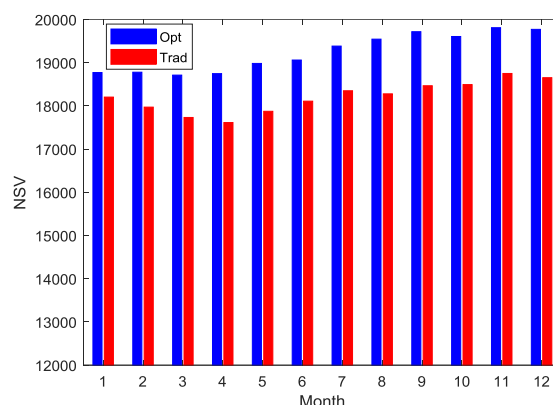


**Figure 3** Comparison results of the number of signals passing through voxel between the traditional method and the optimized method. Opt refers to the optimized method; Trad refers to the traditional method.

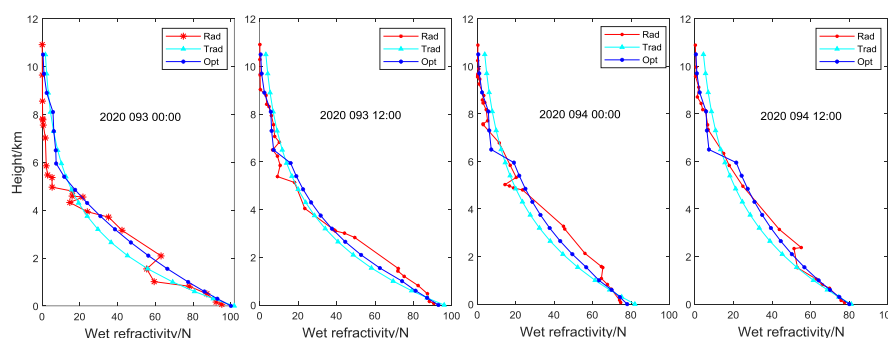


**Figure 4.** Wet refractivity obtained from tomography-derived and radiosonde-derived data. Rad is the wet refractivity derived using radiosonde products, Trad is the wet refractivity derived using the traditional tomography method, and Opt is the wet refractivity derived using the optimized method.

As shown in Fig.3, the average number of NSVs per month of the optimized method is higher than that of the traditional method. From August to December, the average monthly NSVs of the optimized tomography is more than a thousand signals than the traditional tomography. Statistics show that the NSVs in the optimized technique is 5.8% better than that of the traditional technique. As can be seen in Fig. 4, there is a good agreement between the changing trends of wet refractivity with height across the tomography-obtained and data from radiosonde. However, in the case when the "inversion layer" is present, GNSS tomography fails to accurately represent in this situation. The wet refractivity derived from our optimized method is better than that from the traditional method since the blue curve is closer to the red curve. In Table 2, we present the deviation statistics for GNSS tomography-obtained and radiosonde-obtained wet refractivity over the whole year 2016.

**Table 2.** The statistical results between tomography-derived and radiosonde-derived wet refractivity (Unit: N).

Season	Rad-Trad				Rad-Opt			
	Max	Min	Mean	RMS	Max	Min	Mean	RMS



Spring	10.53	-20.31	-3.92	7.66	9.21	-16.36	-2.31	5.89
Summer	19.70	-23.53	-4.82	10.17	14.66	-18.54	-3.56	8.14
Autumn	11.15	-21.05	-3.09	9.03	9.95	-17.24	-3.05	7.82
Winter	10.73	-13.77	0.46	5.64	9.15	-11.95	-1.25	5.03

Table 2 provides statistical values of the differences between GNSS tomography-obtained and radiosonde-obtained results. As seen from the statistical results, the root mean square (RMS) and mean values of troposphere tomography using the optimized technique is less than that of the traditional method. Especially in summer, the optimized method is slightly better than other seasons. In addition, compared with the radiosonde data, the test results show that the wet refractivity quality obtained by the optimized technique is 16.8% better than that of the traditional technique.

#### 4.2 Validation of temperature results

After obtaining the wet refractivity profile based on the GNSS tomography method, the temperature was estimated by the optimal search method using equations (6), (7) and (8). The fifth-generation reanalysis model (ERA5) could provide temperature and water vapor partial pressure, which were selected as the initial values in this study. Since the temperature and water vapor pressure provided by ERA5 are inconsistent with the spatial and temporal resolution of the tomographic results, the Gaussian distance weighting function in the horizontal direction and the exponential function in the vertical direction are used to interpolate ERA5 to be consistent with them. In terms of time, the temperature and water vapor partial pressure of ERA5 can be interpolated by the Chebyshev function of order 9, which can achieve a time resolution consistent with the tomography results. Since our research area is Hong Kong, China, and the tallest building in this area is not more than 600m, we only calculated the temperature at the vertices of each grid layer below 600m. If determining the appropriate search range, it is crucial to find the range of percentage deviation between benchmark value and ERA5 product. Then, using the radiosonde product as the benchmark value, calculate the difference between the temperature and water vapor partial pressure provided by ERA5 and the radiosonde product below 600m. This deviation can be formulated as follows:

$$DT = \frac{RADT-ERAT}{RadT} \cdot 100 \quad (18)$$

$$DWP = \frac{RADWP-ERAWP}{RadWP} \cdot 100 \quad (19)$$

where, the RADT and RADWP are the temperature and pressure provided by radiosonde, respectively, and the ERAT and ERAWP are the temperature and pressure provided by ERA5, respectively. To study the range of percentage deviation of DT and DWP, we computed the situation in Hong Kong from 2010 to 2019 based on Equations (18) and (19).

**Table 3.** Summary of the change intervals of temperature and water vapor pressure between ERA5 and Radiosonde from 2010 and 2019.

DT				DWP	
[-0.75%,0.75%]	[-1%,1%]	[-1.5%,1.5%]	[-7.5%,7.5%]	[-10%,10%]	[-15%,15%]
64.5%	77.7%	93.5%	46.5%	59.2%	71.4%

Table 3 provides the statistics on the scope of DT and DWP in Hong Kong. If the ranges of DT and DWP are too large, some of the temperature and water vapor partial pressure may be over-corrected, but if the range of DN is too small, the temperature and water vapor partial pressure may be under-



corrected. In this study,  $[-0.75\%, 0.75\%]$  in temperature and  $[-10\%, 10\%]$  in water vapor partial pressure are selected as the range of theoretical retrieval. Then, the theoretically retrieved value of atmospheric temperature is obtained at each layer as  $CT + CT \cdot DT$ , where the search step size of DN is 0.25%. The theoretically retrieved value of atmospheric water vapor partial pressure is obtained at each layer as  $CWP + CWP \cdot DWP$ , where the search step size of DN is 2.5%. Finally, the optical  $CT + CT \cdot DT$  values are derived based on the equations (6), (7) and (8). Figure 5 gives the 3-D temperature distribution on Hong Kong below 600m on April 2 and 3, 2020.

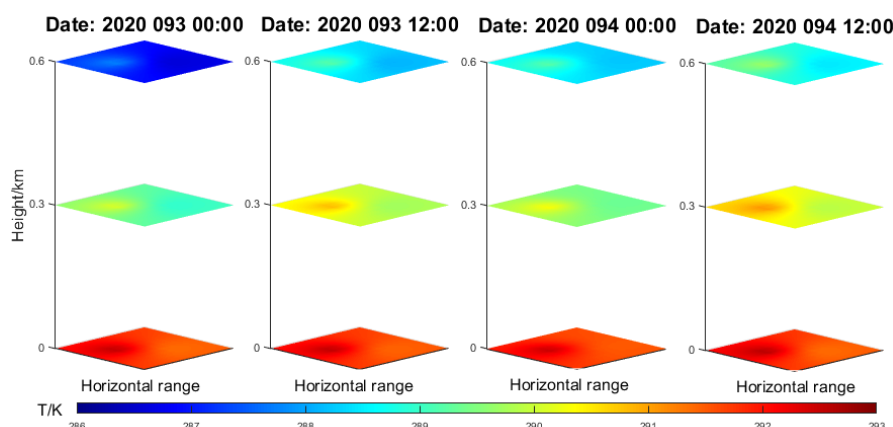


**Figure 5.** 3-D distribution of atmospheric temperature below 600m on April 2 and 3, 2020.

Figure 5 describes the water vapor density changes at different heights. It shows that the atmospheric temperature tends to decrease significantly with elevation. In the horizontal direction, the temperature of the first layer does not change significantly over time, while the temperature of the second and third layers changes more obviously over time. In order to verify the accuracy of the inversion results of the temperature and water vapor pressure, we selected the radiosonde products in 2020 as the true value, and compared them with the inversion results corresponding to time and space. The statistical results are shown in Table 4:

**Table 4.** Statistical results between GNSS-derived and radiosonde-derived temperature and water vapor partial pressure below 600m.

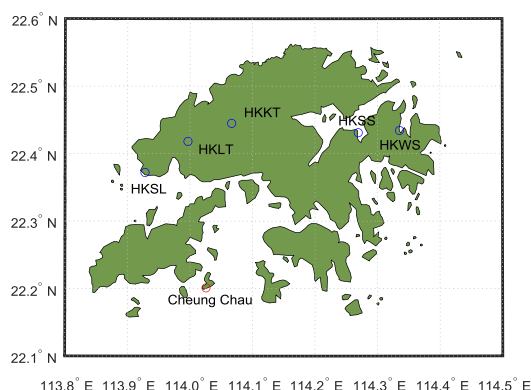
Season	datT (K)				datWV(hPa)			
	Max	Min	Mean	RMS	Max	Min	Mean	RMS
Spring	3.65	-2.17	0.39	1.32	3.66	-2.52	0.72	1.53
Summer	2.56	-2.75	-0.46	1.65	4.12	-3.25	0.48	1.98
Autumn	1.91	-2.52	-0.54	0.96	3.54	-2.54	-0.67	1.47
Winter	3.28	-1.94	0.82	1.45	3.05	-2.33	1.13	1.31

Table 4 provides the different maxima, minima, means and RMSs of GNSS-derived and radiosonde-derived temperatures and water vapor partial pressures. In terms of the statistical results, the accuracy of GNSS-derived temperature and water vapor partial pressure in autumn is better than other seasons. In addition, the best statistical accuracy of GNSS-derived water vapor partial pressure is in winter while the worst is in summer. This can be attributed to summer and winter usually being the most and least humid seasons of the year, respectively.



### 4.3 The urban heat island (UHI)

The UHI intensity is defined by the difference between the temperature in urban areas and surrounding rural areas. In urban areas, anthropogenic sources of heat are present, such as transportation and air conditioning equipment. In contrast, the quantity and variety of anthropogenic heat sources are less in rural areas because there are few existing buildings and most of them are occupied by nature. It is common for rural and urban areas to be interdependent, with rural areas located outside of urban or city areas (Memon et al., 2009). In order to monitor the intensity of the UHI in Hong Kong, we selected several GNSS stations in the urban area (equipped with meteorological observation) as urban stations, and a weather station as a rural station which is located on a surrounding independent island. The distribution of the stations is shown below:



**Figure 6** Distribution of selected GNSS stations and weather stations in Hong Kong. The blue circle indicates the GNSS station, red circle indicates the weather station.

The daily maximum, minimum and average values have been obtained with meteorological data. We fitted these values into a second-order linear function separately. Thus, the maximum, minimum and average values of the UHI intensity in meteorological data were calculated using Eq. (10). In addition, in order to validate the UHI intensity in GNSS data, the temperature obtained by GNSS was interpolated to a same spatial and temporal resolution as the meteorological data using a linear function. Similarly, the maximum, minimum and average of the UHI intensity in GNSS data were calculated using Eq. (9). The results of one of the meteorological stations and the GNSS results that matched with meteorological stations are shown in Figure 7 and Figure 8, respectively.

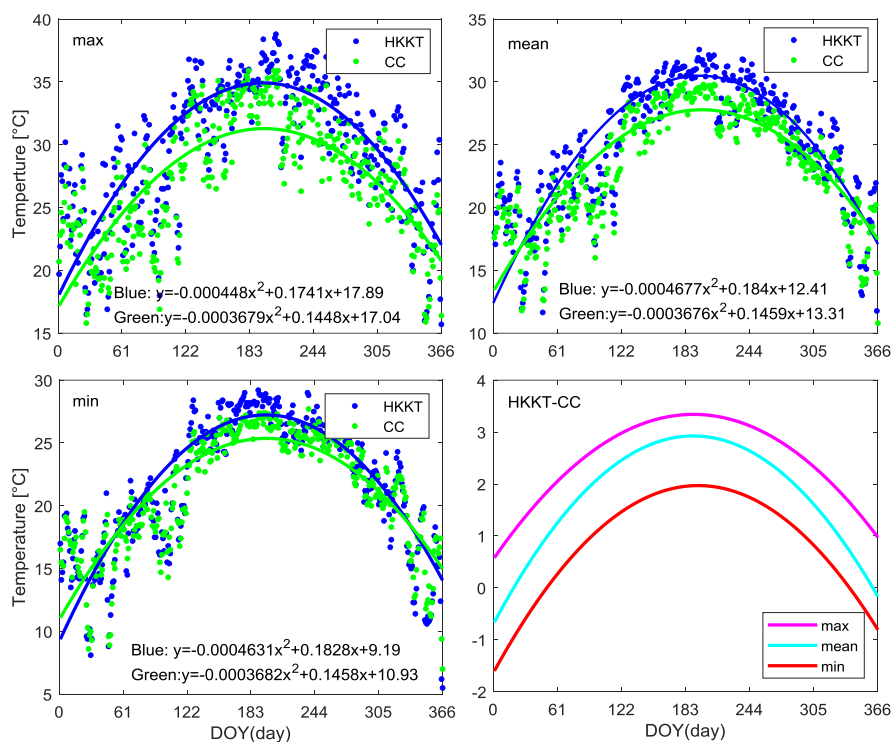


**Figure 7** UHI intensity estimated with meteorological data between HKKT station and CC station. CC refers to Cheung Chau station.

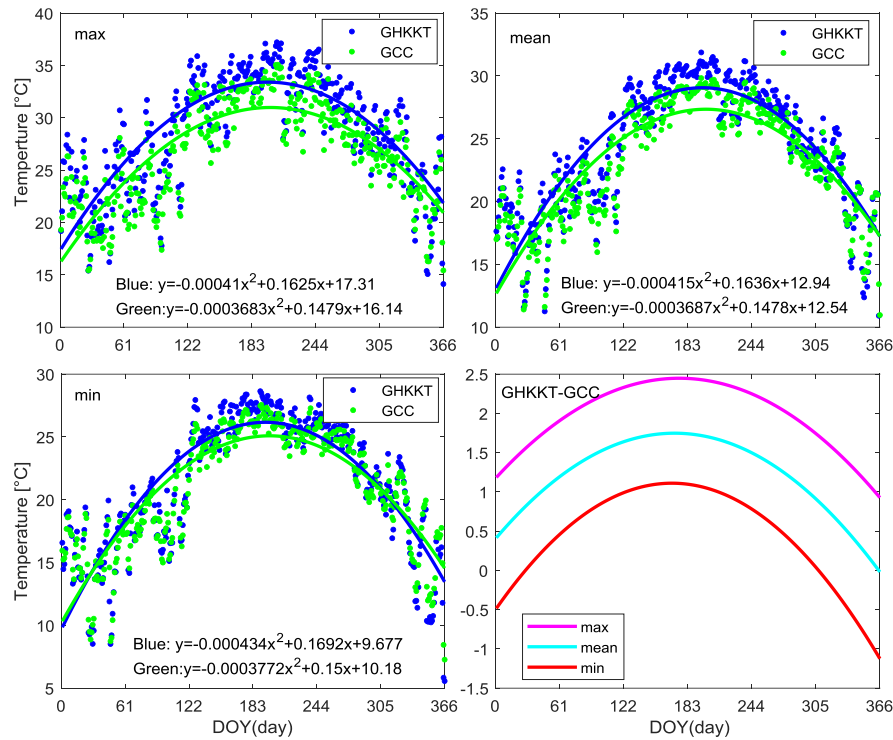


**Figure 8** UHI intensity estimated with ground-based on GNSS observation data. GHKKT refers to the GNSS-derived temperature matched with HKKT meteorological stations. GCC refers to the GNSS-derived temperature matched with Cheung Chau meteorological stations.

The range of the UHI intensity obtained with meteorological data and GNSS data between HKKT and CC is shown in Figure 7 and Figure 8. The shape of the graphs obtained using both data is very similar. In summer, the UHI intensity increases compared to winter. In addition, compared with meteorological data-derived UHI, the UHI obtained from GNSS data is smaller. Beyond that, the 5 pairs of meteorological and GNSS data were used for validation purposes, and the Root Mean Square of the differences between rural and urban areas from meteorological data and GNSS data in different seasons are shown in Table 5 and Table 6. Finally, the validation of the algorithm had been carried out by comparing the UHI intensity (UHII) which determined from GNSS data ( $UHII_{GNSS}$ ) with the UHII which calculated from temperature sensors at weather stations ( $UHII_{met}$ ). The difference in intensity on a given day of the year ( $Diff\_UHII(DOY)$ ) had been compared using the following simple calculation:

$$Diff\_UHII(DOY) = UHII_{GNSS}(DOY) - UHII_{met}(DOY) \quad (20)$$

The RMS values of the differences of the results obtained from GNSS and from meteorological which using both all data and seasonal data are shown in Table 8. The RMS values of the differences were used to validate the algorithm. The 5 pairs of meteorological and GNSS data used for validation purposes are clearly related to location, as described in Table 7.

**Table 5.** Average UHI intensity from each season obtained using meteorological data in 2020 (Unit: K).

Pair of stations	1-year data	Spring	Summer	Autumn	Winter
------------------	-------------	--------	--------	--------	--------



HKKT-CC	1.74	1.99	1.94	1.64	1.36
HKLT-CC	1.44	1.54	1.49	1.32	1.40
HKSL-CC	1.39	1.51	1.46	1.24	1.31
HKSS-CC	1.37	1.44	1.41	1.22	1.39
HKWS-CC	1.53	1.59	1.55	1.46	1.53

**Table 6.** Average UHI intensity from each season obtained using GNSS data in 2020 (Unit: K).

Pair of stations	1-year data	Spring	Summer	Autumn	Winter
GHKKT-GCC	1.22	1.33	1.28	1.19	1.22
GHKLT-GCC	1.06	1.18	1.05	0.96	1.06
GHKSL-GCC	1.11	1.19	1.13	1.01	1.06
GHKSS-GCC	0.93	1.05	0.92	0.85	0.87
GHKWS-GCC	0.98	1.08	0.96	0.82	0.97

**Table 7.** Relation of meteorological and GNSS pairs.

	Meteorological data	GNSS data
UHII1	HKKT-CC	GHKKT-GCC
UHII2	HKLT-CC	GHKLT-GCC
UHII3	HKSL-CC	GHKSL-GCC
UHII4	HKSS-CC	GHKSS-GCC
UHII5	HKWS-CC	GHKWS-GCC

**Table 8.** RMS of the differences between UHI intensity obtained with meteorological data and GNSS data in Hong Kong in 2020 (Unit: K).

Pair of stations	1-year data	Spring	Summer	Autumn	Winter
UHII1	1.34	1.45	1.36	1.31	1.25
UHII2	1.03	1.12	1.03	0.96	1.03
UHII3	1.05	1.16	1.05	0.98	0.93
UHII4	1.13	1.21	1.10	1.08	1.03
UHII5	1.23	1.32	1.24	1.14	1.25

The tables 5 and 6 show the mean UHI intensity of meteorological data and GNSS data in 2020 using 1-year data and data for each season. In all cases, the UHI intensity is the highest during spring, and the lowest during autumn. The mean UHI intensity in different seasons is less than 0.6 K at the same station while the mean UHI intensity of one-year data is less than 0.4K. As shown in Figure 8, all RMS of the differences between the UHII obtained with GNSS data and meteorological data are below 1.5K. In addition, compared with meteorological data, the accuracy of the UHI intensity is 1.20 K at a 95% confidence level using a full year of GNSS data.

## 5. Conclusion

GNSS radio occultation provides high-precision middle and upper atmospheric parameter profiles (pressure, water vapor partial pressure and temperature). In this paper, historical radiosonde data and radio occultation data were used to optimize the ground-based GNSS tomography model to improve the accuracy of tomography-derived wet refractivity. After obtaining the wet refractivity,



the ERA5 product was used as the initial value, and the search method was used to obtain the best temperature for the wet refractivity. The developed algorithm demonstrated the possibility of using GNSS data to monitor the UHI intensity. Ground-based GNSS data can be used for micro and meso-scale urban climate studies and has the following advantages: 1). the ground-based GNSS tomography technique works in all weather conditions, and its data are widely available as GNSS constellations are designed to cover the earth at all times; 2). GNSS data has a very high temporal resolution and can be processed in real-time or near-real-time.

This study overcomes two major challenges in the algorithm development. The first challenge is the determination of the GNSS tomographic top grid height. Here, we obtained the SGT and FGT based on the RO data and radiosonde products in Hong Kong, and fitted the wet refractivity between FGT and SGT to a multi-order spherical harmonic function based on historical radiosonde and RO products. The height between the earth's surface and SGT was divided into several voxels, and the wet refractivity at the vertex of the voxels was used as an unknown parameter for GNSS tomography. While several voxels are also divided between SGT and FGT, and the wet refractivity at the vertex of voxels was directly obtained based on Eq. (16). Thus, the height of the grid top is decreased, conversely increasing the effective number of the GNSS satellite rays. Moreover, the number of unknowns in GNSS tomography can be reduced, and the accuracy of the tomography results can be improved.

The second challenge is the estimation of temperature from wet refractivity. Based on the relationship between wet refractivity and temperature and water vapor partial pressure, as well as the linear variation of temperature with elevation and the approximate exponential change of water vapor partial pressure with elevation, the optimal search method was used to obtain water vapor partial pressure and temperature from wet refractivity. After selecting five meteorological observing stations inside the city of Hong Kong as urban stations, and a station on an island in Hong Kong as a rural station, we used Eq. (10) to estimate the UHII as the benchmark value of the UHII obtained from GNSS data.

Using the data of 18 stations in Hong Kong in 2020 for a trial calculation, the following conclusions are obtained:

- (1) Compared with the radiosonde data, the test results show that the wet refractivity quality obtained by the optimized technique is 16.8% better than that obtained by the traditional technique.
- (2) Using the radiosonde product as the benchmark value, the accuracy of the temperature obtained by GNSS data below 600 meters is better than 1.35K.
- (3) By solving the RMS of the differences between UHII obtained from GNSS data and meteorological data on the 5 selected locations, it has been shown that, the difference of the UHII obtained from GNSS data and the measured UHII using temperature data in spring and summer is higher than other seasons, because the water vapor content is more abundant in these two seasons. Therefore, the water vapor partial pressure is not accurately calculated in spring and summer. The discrepancies between the HUI estimated by the algorithm and the UHII obtained from meteorological stations can be attributed to the lack of water vapor partial pressure data and GNSS processing. The new algorithm can be used to monitor the diurnal cycle of the UHI.

#### **Data Availability**



488 The radiosonde observations (IGRA2, 2022) can be downloaded from the following website:  
489 <https://www1.ncdc.noaa.gov/pub/data/igra.html>. In addition, the fifth generation of the European  
490 Centre for Medium-Range Weather Forecasts (ECMWF) reanalysis (ERA5,2022) can also be  
491 collected free of charge from <https://apps.ecmwf.int/datasets/data/interim-full-daily>. WEGC GNSS  
492 RO OPSv5.6 data are supported by the WEGC EOPAC team and are available online (see  
493 <https://doi.org/10.25364/WEGC/OPS5.6:2021.1>)

#### 494 Reference

- 495 Anthes, R. A., Bernhardt, P. A., Chen, Y., Cucurull, L., Dymond, K. F., Ector, D., Healy, S. B., Ho,  
496 S. P., Hunt, D. C., Kuo, Y. H., Manning, K., and McCormick, C. 2008. The  
497 COSMIC/FORMOSAT-3 mission: early results. B. Am. Meteorol. Soc. 89: 1-21.  
498 <https://doi.org/10.1175/BAMS-89-3-313>
- 499 Azevedo, I. and Leal, V.M.S. 2017. Methodologies for the evaluation of local climate change  
500 mitigation actions: a review. Renew Sustain Energy Rev., 79: 681-690.  
501 <https://doi.org/10.1016/j.rser.2017.05.100>
- 502 Benevides, P., Catalao, J. and Miranda, P. M. A. 2015. On the inclusion of GPS precipitable water  
503 vapour in the nowcasting of rainfall. Nat. Hazard Earth Sys. 15: 2605-2616.  
504 <https://doi.org/10.5194/nhess-15-2605-2015>
- 505 Benevides, P., Nico, G., Catalão, J., and Miranda, P. M. A. 2016. Bridging InSAR and GPS  
506 Tomography: A New Differential Geometrical Constraint. IEEE T. Geosci. Remote. 54: 697-702,  
507 <https://doi.org/10.1109/TGRS.2015.2463263>
- 508 Bender, M. and Raabe, A. 2007. Preconditions to ground based GPS water vapour tomography.  
509 Ann. Geophys. 25: 1727-1734. <https://doi.org/10.5194/angeo-25-1727-2007>
- 510 Bender, M., Dick, G., Ge, M., Deng, Z., Wickert, J., Kahle, H.-G., Raabe, A., and Tetalaiff, G. 2011.  
511 Development of a GNSS water vapour tomography system using algebraic reconstruction  
512 techniques. Adv. Space Res. 47: 1704-1720. <https://doi.org/10.1016/j.asr.2010.05.034>
- 513 Cai, C. and Gao, Y. 2013. Modeling and assessment of combined GPS/GLONASS precise point  
514 positioning. GPS Solut. 17 (2):223-236. <https://doi.org/10.1007/s10291-012-0273-9>
- 515 Cai, C., Gao, Y., Pan, L. and Zhu, J. 2015. Precise point positioning with quad-constellations: GPS,  
516 BeiDou, GLONASS and Galileo. Adv. Space Res. 56 (1): 133-143. <https://doi.org/10.1016/j.asr.2015.04.001>
- 517 Callahan, P. Prediction of Tropospheric Wet-Component Range Error from Surface Measurements;  
518 JPL Technical Report 32-1526; Jet Propulsion Laboratory, California Institute of Technology:  
519 Pasadena, CA, USA, 1973.
- 521 Chen, B. Y. and Liu, Z. Z. 2014. Voxel-optimized regional water vapor tomography and comparison  
522 with radiosonde and numerical weather model, J. Geodesy, 88: 691-703.  
523 <https://doi.org/10.1007/s00190-014-0715-y>
- 524 Fang, X., Zou, B., Liu, X., Sternberg, T. and Zhai, L. 2016. Satellite-based ground PM2.5 estimation  
525 using timely structure adaptive modeling. Remote Sens Environ. 186: 152-163. <https://doi.org/10.1016/j.rse.2016.08.027>
- 526 Flores, A., Ruffini, G. and Rius, A. 2000. 4D tropospheric tomography using GPS slant wet delays,  
527 Ann. Geophys. 18: 223-234. <https://doi.org/10.1007/s00585-000-0223-7>
- 528 Foster, J., Bevis, M., and Businger, S. 2005. GPS meteorology: sliding window analysis. J. Atmos.  
529 Ocean. Tech. 22: 687-695. <https://doi.org/10.1175/JTECH1717.1>
- 530



- 531 Herring, T. A., King, R. W., and McClusky, S. C. 2010. GAMIT Reference Manual Release 10.4,  
532 Department of Earth, Atmospheric, and Planetary Sciences, Massachusetts Institute of  
533 Technology, available at: [http://www-gpsg.mit.edu/~simon/gtgk/GAMIT\\_Ref.pdf](http://www-gpsg.mit.edu/~simon/gtgk/GAMIT_Ref.pdf). last access: 14  
534 August 2021.
- 535 Jauregui, E. 1997. Heat island development in Mexico city. *Atmos. Environ.* 31(22): 3821-3831.  
536 [https://doi.org/ 10.1016/S1352-2310\(97\)00136-2](https://doi.org/10.1016/S1352-2310(97)00136-2)
- 537 Jiang, X., Zou, B., Feng, H., Tang, J., Tu, Y. and Zhao, X. 2019. Spatial distribution mapping of Hg  
538 contamination in subclass agricultural soils using GIS enhanced multiple linear regression. *J*  
539 *Geochem Explor.* 196: 1-7. <https://doi.org/10.1016/j.gexplo.2018.10.002>
- 540 Jin, M.S. 2012. Developing an index to measure urban heat island effect using satellite land skin  
541 temperature and land cover observations. *J. Clim.* 25(18): 6193-6201. [https://doi.org/](https://doi.org/10.1175/JCLI-D-11-00509.1)  
542 [10.1175/JCLI-D-11-00509.1](https://doi.org/10.1175/JCLI-D-11-00509.1)
- 543 Jiang, P., Ye, S. R., Liu, Y. Y., Zhang, J. J. and Xia, P. F. 2014. Near realtime water vapor tomography  
544 using ground-based GPS and meteorological data: long-term experiment in Hong Kong, *Ann.*  
545 *Geophys.* 32: 911-923. <https://doi.org/10.5194/angeo-32-911-2014>
- 546 Jorge, M.A., Lawrence, L. Tang, Y.T. and Terry, M. 2021. A new global navigation satellite system  
547 (GNSS) based method for urban heat island intensity monitoring. *International Journal of Applied*  
548 *Earth Observations and Geoinformation.* 94: 102222. <https://doi.org/10.1016/j.jag.2020.102222>
- 549 Kayet, N., Pathak, K., Chakrabarty, A. and Sahoo, S. 2016. Spatial impact of land use/land cover  
550 change on surface temperature distribution in Saranda Forest, Jharkhand. *Model Earth Syst*  
551 *Environ.* 2(3): 127. <https://doi.org/10.1007/s40808-016-0159-x>
- 552 Kouba, J. and Héroux, P. 2001. Precise point positioning using IGS orbit and clock products. *GPS*  
553 *Solut.* 5 (2): 12-28. <https://doi.org/10.1007/pl00012883>
- 554 Kishore, P., Venkat R. M., Namboothiric, S. P., Velicognaa, I., Bashab, G., Jiang, J. H., Igarashi, K.,  
555 Rao, S. V. B., and Sivakumar, V. 2011. Global (50 S–50 N) Distribution of water vapour observed  
556 by Cosmic GPS Ro: comparison with GPS Radiosonde, NCEP, Era-Interim, and Jra-25 reanalysis  
557 data sets. *J. Atmos. Sol.-Terr. Phy.*, 73: 1849-1860. [https://doi.org/ 10.1016/j.jastp.2011.04.017](https://doi.org/10.1016/j.jastp.2011.04.017)
- 558 Kuo, Y. H., Schreiner, W. S., Wang, J., Rossister, D. L., and Zhang, Y. 2005. Comparison of GPS  
559 radio occultation soundings with radiosondes. *Geophys. Res. Lett.* 32: L05817.  
560 <https://doi.org/10.1029/2004GL021443>
- 561 Lamarca, C., Qüense, J. and Henríquez, C. 2018. Thermal comfort and urban canyons morphology  
562 in coastal temperate climate, Concepción, Chile. *Urban Climate.* 23: 159-172. [https://doi.org/](https://doi.org/10.1016/j.uclim.2016.10.004)  
563 [10.1016/j.uclim.2016.10.004](https://doi.org/10.1016/j.uclim.2016.10.004)
- 564 Niell, A. E. 1996. Global mapping functions for atmosphere delay at radio wavelengths. *J. Geophys.*  
565 *Res.* 101: 3227-3246. [https://doi.org/ 10.1029/95JB03048](https://doi.org/10.1029/95JB03048)
- 566 Memon, R.A., Leung, D. Y. C. and Liu, C.H. 2009. An investigation of urban heat island intensity  
567 (UHII) as an indicator of urban heating. *Atmos. Res.* 94(3), 491-500.  
568 <https://doi.org/10.1016/j.atmosres.2009.07.006>
- 569 Peng, F., Wong, M.S., Wan, Y.L. and Nichol, J.E. 2017. Modeling of urban wind ventilation using  
570 high resolution airborne LiDAR data. *Computers. Environment and Urban Systems.* 64: 81-90.  
571 <https://doi.org/10.1016/j.compenvurbsys.2017.01.003>
- 572 Perler, D., Geiger, A., and Hurter, F. 2011. 4D GPS water vapour tomography: new parameterized  
573 approaches. *J. Geophys.*, 85: 539-550. <https://doi.org/10.1007/s00190-011-0454-2>
- 574 Ramamurthy, P. and Sangobanwo, M. 2016. Inter-annual variability in urban heat island intensity



- 575 over 10 major cities in the United States. *Sustain. Cities Soc.* 26: 65-75.
- 576 <https://doi.org/10.1016/j.scs.2016.05.012>
- 577 Rizwan, A.M., Dennis, L.Y.C, Liu, C. 2018. A review on the generation, determination and
- 578 mitigation of Urban Heat Island. *J. Environ. Sci.* 20(1): 120-128. [https://doi.org/10.1016/s1001-](https://doi.org/10.1016/s1001-0742(08)60019-4)
- 579 [0742\(08\)60019-4](https://doi.org/10.1016/s1001-0742(08)60019-4)
- 580 Rohm, W. 2012. The precision of humidity in GNSS tomography. *Atmos. Res.*, 107, 69-75.
- 581 <https://doi.org/10.1016/j.atmosres.2011.12.008>
- 582 Rohm, W. 2013. The ground GNSS tomography-unconstrained approach. *Adv. Space Res.*, 51, 501-
- 583 513. <https://doi.org/10.1016/j.asr.2012.09.021>
- 584 Roth, M. 2013. Urban heat island. In: Fernando, H.J.S. (Ed.), *Handbook of Environmental Fluid*
- 585 *Dynamics*. Vol. II. Taylor & Francis Group. pp. 143-159.
- 586 Schreiner, W., Rochen, C., Sokolovskiy, S., Syndergaard, S., and Hunt, D. 2007. Estimates of the
- 587 precision of GPS radio occultation from the COSMIC/FORMOSAT-3 mission. *Geophys. Res.*
- 588 *Lett.* 34:L04808. <https://doi.org/10.1029/2006GL027557>
- 589 Schwarz, N., Lautenbach, S. and Seppelt, R. 2011. Exploring indicators for quantifying surface
- 590 urban heat islands of European cities with MODIS land surface temperatures. *Remote Sens*
- 591 *Environ.* 115(12): 3175-3186. <https://doi.org/10.1016/j.rse.2011.07.003>
- 592 Song, S. L. 2004. Sensing three dimensional water vapor structure with Ground-based GPS network
- 593 and the application in meteorology. PhD thesis of Shanghai Astronomical Observatory CAS. 80-
- 594 84, 2004.
- 595 Troller, M., Geiger, A., Brockmann, E., and Kahle, H.-G. 2006. Determination of the spatial and
- 596 temporal variation of tropospheric water vapor using CGPS networks. *Geophys J. Int.*, 167, 509-
- 597 520, 2006. <https://doi.org/10.1111/j.1365-246X.2006.03101.x>
- 598 Wu, H., Ye, L. P., Shi, W.Z. and Clarke, K. C. 2014. Assessing the effects of land use spatial structure
- 599 on urban heat islands using HJ-1B remote sensing imagery in Wuhan, China. *International Journal*
- 600 *of Applied Earth Observation and Geoinformation*, 32(1): 67-78.
- 601 <https://doi.org/10.1016/j.jag.2014.03.019>
- 602 Xia, P., Cai, C. and Liu, Z. 2013. GNSS troposphere tomography based on two-step reconstructions
- 603 using GPS observations and COSMIC profiles. *Ann. Geophys.*, 31: 1805-1815.
- 604 <https://doi.org/10.5194/angeo-31-1805-2013>
- 605 Xia, P.F., Ye, S.R., Jiang, P., Pan, L. and Guo, M. 2018. Assessing water vapor tomography in Hong
- 606 Kong with improved vertical and horizontal constraints. *Annales Geophysicae*. 36: 969-978.
- 607 <https://doi.org/10.5194/angeo-36-969-2018>
- 608 Xu, S., Zou, B., Shafi, S and Sternberg, T. 2018. A hybrid Grey-Markov/ LUR model for PM10
- 609 concentration prediction under future urban scenarios. *Atmos Environ*, 187: 401-409.
- 610 <https://doi.org/10.1016/j.atmosenv.2018.06.014>
- 611 Vahmani, P. and Ban-Weiss, G.A. 2016. Impact of remotely sensed albedo and vegetation fraction
- 612 on simulation of urban climate in WRT-urban canopy model: a case study of the urban heat island
- 613 in Los Angeles. *J. Geophys. Res. Atmos.* 121 1511-1531. <https://doi.org/10.1002/2015JD023718>
- 614 Zhai, L., Zou, B., Fang, X., Luo, Y., Wan, N. and Li, S. 2016. Land use regression modeling of
- 615 PM2.5 concentrations at optimized spatial scales. *Atmos*, 8(1): 1.
- 616 <https://doi.org/10.1016/j.scitotenv.2020.140744>
- 617 Zou, B., You, J., Lin, Y., Duan, X., Zhao, X., Xin, F., Campen, M. J. and Li, S. 2019. Air pollution
- 618 intervention and life-saving effect in China. *Environ Int.* 125: 529-541.



619 <https://doi.org/10.1016/j.envint.2018.10.045>

620

621 **Author contributions.**

622 P. Xia, P. Wei, and S. Ye contributed to the conception of the study;

623 P. Xia, P. Wei, S. Ye, and M. Guo performed the experiment;

624 P. Xia, P. Wei, S. Ye, and F. Hu contributed significantly to analysis and manuscript preparation;

625 P. Xia, P. Wei, and F. Hu performed the data analyses and wrote the manuscript;

626 P. Xia, S. Ye, and M. Guo helped perform the analysis with constructive discussions.

627

628 **Competing interests.**

629 The authors declared that they have no conflicts of interest to this work.

630 We declare that we do not have any commercial or associative interest that represents a conflict  
631 of interest in connection with the work submitted.

632

633